

1 **Increasing risk of another Cape Town “Day Zero” drought in the twenty-**
2 **first century**

3
4 Salvatore Pascale^{1,2,3*}, Sarah B. Kapnick², Thomas L. Delworth², William F. Cooke²

5 ¹ *Department of Earth System Science, Stanford University, Stanford CA*

6 ² *NOAA/Geophysical Fluid Dynamics Laboratory, Princeton NJ*

7 ³ *Atmospheric and Ocean Sciences Program, Princeton University, Princeton, NJ*

8 * **Corresponding author:** To whom correspondence should be addressed. Salvatore Pas-
9 cale, E-mail: pascaledeep@gmail.com

Abstract

10

11 Three consecutive dry winters (2015-2017) in southwestern South Africa (SSA) resulted in
12 the Cape Town “Day Zero” drought in early 2018. The contribution of anthropogenic global
13 warming to this prolonged rainfall deficit has previously been evaluated through observations
14 and climate models. However, model adequacy and insufficient horizontal resolution make it
15 difficult to precisely quantify the changing likelihood of extreme droughts given the small re-
16 gional scale. Here we use a new high-resolution large ensemble to estimate the contribution
17 of anthropogenic climate change to the probability of occurrence of multi-year SSA rainfall
18 deficits in past and future decades. We find that anthropogenic climate change increased
19 the likelihood of the 2015-2017 rainfall deficit by a factor of five-to-six. The probability of such
20 an event will increase from 0.7% to 25% by the year 2100 under an intermediate-emission
21 scenario (SSP2-4.5) and to 80% under a high-emission scenario (SSP5-8.5). These results
22 highlight the strong sensitivity of the drought risk in SSA to future anthropogenic emissions.

Significance Statement

24 The Cape Town “Day Zero” drought was caused by an exceptional three-year rainfall deficit.
25 Through the use of a higher resolution climate model, our analysis further constrains previ-
26 ous work showing that anthropogenic climate change made this event five-to-six times more
27 likely relative to early 20th century. Furthermore, we provide a clear and well-supported
28 mechanism for the increase in drought risk in SSA through a dedicated analysis of the cir-
29 culation response, which highlights how – as in 2015-17 – a reduction in precipitation during
30 the shoulder seasons is likely to be the cause of drought risk in SSA in the 21st century.
31 Overall, this study greatly increases our confidence in the projections of a drying SSA.

32 The Day Zero Cape Town drought was one of the worst water crises ever experienced
33 in a metropolitan area^{1,2}. Droughts are a regular occurrence in SSA, having occurred dur-
34 ing the late 1920s, early 1970s, and more recently during 2003-2004 (Fig. 1a,b). However,
35 the extended winter (April-September, AMJJAS) three-year rainfall deficit (Fig. 1a-b; SI Ap-
36 pendix, Fig. S1) which drove the 2015-2017 Cape Town drought²⁻⁸ was exceptional over the
37 last century^{4,9}. Storage in reservoirs supplying water to 3.7 million people in the Cape Town
38 metropolitan area dropped to about 20% of capacity in May 2018. As a consequence, strict
39 water usage restrictions were implemented to delay water levels reaching 13.5%, the level
40 at which much of the city's municipal supply would have been disconnected⁷, a scenario re-
41 ferred to as "Day Zero" by the municipal water authorities⁷. Above average winter rain over
42 the rest of the 2018 austral winter allowed Cape Town to avoid the Day Zero scenario.

43 While poor water management practices and infrastructure deficiencies worsened the
44 crisis^{10,11}, the 2015-2017 rainfall deficit was the main driver of the drought⁵. To facilitate the
45 improvement of water management practices and the infrastructure necessary to make the
46 system more resilient, it is critical to first determine how likely a meteorological drought like
47 the one in 2015-2017 might be in the coming decades. Increased aridity is expected in most
48 of southern Africa¹²⁻¹⁴ as a consequence of the Hadley Cell poleward expansion^{4,15-18} and
49 southward shift of the Southern Hemisphere jet stream¹⁹. Second, the risk of more extreme
50 droughts should be quantified to understand the potential for emerging risks that could make
51 a Day Zero event in Cape Town unavoidable.

52 Previous work⁵ has suggested that the Day Zero drought may have been made 1.4-
53 to-6.4 times more likely over the last century due to +1 K of global warming, with the risk
54 expected to scale linearly with one additional degree of warming. Such estimates make
55 use of statistical models of the probability distribution's tail (e.g., the Generalized Extreme
56 Value) applied to observations and previous-generation (i.e., as those participating to the
57 Coupled Model Intercomparison Project Phase 3²⁰ and 5²¹) climate models. CMIP3 and

58 CMIP5 models have been shown to have a systematically biased position of the Southern
59 Hemisphere jet stream toward the equator due to insufficient horizontal resolution¹⁹. This
60 produces a large uncertainty in model projections of jet stream shifts^{22,23}, thus hindering
61 realistic projections of Southern Hemisphere climate change. Furthermore, for hydroclimatic
62 variables, a statistical extrapolation of the probability distribution's tail might have inherent
63 limitations in providing precise estimates of the event probability of future extreme events,
64 although its precision profits from the use of large ensembles^{24,25}.

65 Large ensembles of comprehensive climate models provide thousands of years of data
66 that allow direct construction of the underlying probability distribution of hydroclimatic ex-
67 tremes without relying on a hypothesized statistical model of extremes^{25,26}. South African
68 winter rains have high interannual and decadal variability due to El Niño-Southern Oscilla-
69 tion²⁷, the Southern Annular Mode²⁸ and interdecadal variability²⁹. A multi-decade to multi-
70 century record may be required to detect the emergence of statistically significant trends in
71 regional precipitation extremes. A large ensemble is thus a powerful method to isolate, at
72 the decadal timescale, internal natural variability (e.g., SI Appendix, Fig. S2) from the forced
73 signal^{30–32}.

74 **The SPEAR large ensemble**

75 To tackle this problem, we use a comprehensive suite of new large ensemble simulations
76 from the newly developed **Seamless System for Prediction and EArth System Research**
77 (SPEAR) global climate model developed³³ at the Geophysical Fluid Dynamics Laboratory
78 (GFDL, see Methods). SPEAR is the latest GFDL modeling system for seasonal to mul-
79 tidecadal prediction and projection, and it shares underlying component models with the
80 CM4³⁴ climate model, which participates to the Coupled Model Intercomparison Project
81 Phase 6 (CMIP6)³⁵. In particular, we use the medium horizontal atmospheric resolution
82 (50 km) version of SPEAR, i.e., SPEAR_MED, which has been designed to study regional

83 climate and extremes. The SPEAR_MED simulations include a 3,000-year preindustrial
84 control simulation (CTRL), and three 30-member ensembles that account for changing at-
85 mospheric compositions arising from natural sources only (NATURAL), and natural plus an-
86 thropogenic sources (HIST+SSP2-4.5, HIST+SSP5-8.5, Methods for details). The relatively
87 high horizontal resolution of SPEAR_MED – which makes this large ensemble unique – is
88 key to better resolve the steep coastal SSA topography, which leads to orographic enhance-
89 ment of rainfall during frontal days⁴. SPEAR_MED is an excellent tool to investigate SSA
90 droughts because it has a realistic representation of the SSA winter rainfall pattern (Fig. 1c-
91 d) and seasonal cycle (Fig. 1f), and it correctly reproduces the amplitude of the interannual,
92 multiannual and decadal natural variability of the SSA winter rainfall (SI Appendix, Fig. S3).

93 **Event attribution to anthropogenic climate change**

94 As anthropogenic global warming weakens the basic stationarity assumption which has his-
95 torically been at the foundation of water management³⁶, two key questions are: to what
96 extent did anthropogenic global warming make the Day Zero drought more likely? And: how
97 will the probability of occurrence of another similar or worse meteorological drought change
98 in the coming decades? To address these questions, we first assess if the probability distri-
99 bution of anomalies of the three-year-mean Winter Rainfall Index (WRI, see Methods) has
100 already significantly changed. We directly compare the time-evolving probability distribution
101 associated with successive twenty-year time windows with that associated with only inter-
102 nal climate variability obtained from a long control run at preindustrial forcing (CTRL; see
103 Methods for details). The two probability distributions are statistically indistinguishable at
104 the 99.9% level per the Kolmogorov-Smirnov test, during the twenty-year period 1980-2000
105 (Fig. 2a), but then start to significantly differ from 1990-2010 onward (Fig. 2b-d). Here-
106 after we refer to the 2015-2017 WRI negative anomaly as “event_1517”. The average of
107 the event_1517 probabilities in the five decades 1921-1970 is approximately 0.7% (Fig. 2e).

108 This is slightly smaller than the value from the 3,000-year preindustrial control run and with
109 the NATURAL experiment (1%) – which profit from the much longer time span (SI Appendix,
110 Fig. S4a) – but nevertheless consistent within the 95% uncertainty interval. The event prob-
111 ability is stationary up to 1980-2000, after which it starts increasing (Fig. 2e). For 2015-2017
112 the event probability – obtained by linear interpolation of the 2000-2020 and 2010-2030 val-
113 ues, is 3.7 % with a [2.5%,4.7%] 95% confidence interval. This implies a risk ratio – i.e., the
114 ratio of the probability of the event at at given time to its probability in the early 20th century
115 – of 5.5 times, with a confidence interval of 4 to 8 (Fig. 2g). Thus, an extreme event that had
116 an average recurrence interval³⁷ of one hundred years in the early 20th century reduces to
117 25-year recurrence interval by present day. This is consistent with previous work⁵ in spite of
118 the different event definition between the two studies.

119 **Drought risk projections**

120 In the high-emission scenario SSP5-8.5 (intermediate-emission scenario SSP2-4.5), the
121 event_1517 probability – i.e., the likelihood that rainfall is below the event_1517 thresh-
122 old for any random three year segment within the twenty-year window – is projected to rise
123 to 20% (13%) around 2045 (Fig 2f and SI Appendix, Figs. S5 and S6) and to reach 80%
124 (25%) by the end of this century. For the SSP5-8.5 (SSP2-4.5) scenario, the likelihood of an
125 event_1517 would thus increase by a factor of 120 (40) relative to earlier in the twentieth-
126 century (Fig. 2h). This implies that the expected number of such droughts in 2081-2100 will
127 be approximately $\text{probability} \times (20 \text{ years} / 3 \text{ years})$, i.e., 5.3 (2.3) under SSP5-8.5 (SSP2-4.5).
128 Extending the finding of previous studies⁵ beyond +2 K of mean global surface temperature
129 increase, we find that, for each degree of warming, the risk ratio grows at a slower rate after
130 a fast, ongoing acceleration (SI Appendix, Fig. S7). This implies a transition to substantially
131 drier and persistent wintertime conditions over SSA.

132 Using the same methodology (see Methods), we can also estimate the distribution and

133 the probability of occurrence of a four-year WRI anomaly at the same intensity of event_1517
134 (Fig. 2i-j). This has not occurred yet but, if it occurred, could lead to an unavoidable Day Zero.
135 In the absence of anthropogenic forcing (i.e., CTRL and NATURAL), such an event has a
136 probability of occurrence of 0.4% (vs. approximately 1% for a three-year drought). Presently,
137 the probability of occurrence for it to happen has already substantially increased relative to
138 the early 20th century (2%), and it is projected to be 15% (8%) by mid-century under SSP5-
139 8.5 (SSP2-4.5). By the end of the 21st century, a four-year WRI anomaly will be almost as
140 likely as three-year rainfall anomaly of intensity comparable to the 2015-2017 event.

141 This suggests that the duration of meteorological droughts will increase in SSA. We esti-
142 mate the probability distribution of the severe (i.e., ≤ -6 mm month⁻¹) winter (i.e., AMJJAS)
143 WRI anomalies as a function of duration and intensity under the SSP2-4.5 (Fig. 3a-c) and
144 SSP5-8.5 scenario (Fig. 3d-f). Historically, the largest (in magnitude) negative WRI anoma-
145 lies typically last 1 year. There is a non-negligible probability of two-to-three-year persisting
146 anomalies at about -10 mm month⁻¹, while anomalies lasting longer than three years are
147 unlikely (Fig. 3). Anthropogenic climate change will make meteorological winter droughts
148 lasting three to ten years more likely and more acute, especially under the SSP5-8.5 sce-
149 nario (Fig. 3d-f).

150 **Large scale circulation shifts**

151 The future increase in the probability of occurrence of intense and prolonged rainfall deficits
152 (Fig. 2f and Fig. 3) is suggestive of a substantial climatic shift in the mean wintertime condi-
153 tions of SSA in the coming decades. In agreement with state-of-the-art general circulation
154 models^{6,38}, SPEAR_MED indicates a substantial AMJJAS WRI reduction during the twenty-
155 first century (SI Appendix, Fig. S8a), especially in the shoulder seasons of April-May and
156 August-October (SI Appendix, Fig. S8b). In both scenarios, the amplitude of the shift will be
157 outside the range of what could occur from low-frequency internal climate variability in the

158 decade 2020-2030 (Fig. 4a-c), but the magnitude of the negative anomaly will be substan-
159 tially larger under a high-emission scenario.

160 The prolonged rainfall deficit experienced during winters 2015-2017 occurred along with
161 positive large scale anomalies in sea level pressure on the southern flank of the South
162 Atlantic and South Indian Subtropical High^{4,18}. Higher sea level pressure has been invoked
163 as the cause of fewer extratropical cyclones over the South Atlantic and of a southward shift
164 of the moisture corridors contributing to winter rainfall³. Other studies⁴ find no significant
165 regional trends over the last forty years in the number of cold fronts making landfall over
166 SSA, but highlight the shorter duration of rainfall events associated with cold fronts due to
167 larger sea level pressure during post-frontal days. Positive significant trends in sea level
168 pressure have been observed in the Southern Hemisphere over the last forty years and
169 have been related to the multidecadal expansion of the Southern Hemisphere's summer and
170 fall Hadley Cell^{15,16,18}. In SPEAR_MED, the forced (i.e., ensemble mean) decadal changes
171 in sea level pressure are visible in the period 1980-2020 (SI Appendix, Fig. S9), with the
172 typical patterns that might dominate at end of the twenty-first century (SI Appendix, Fig. S10)
173 emerging around 2000-2010. This is in agreement with previous studies^{16,17} suggesting that
174 the forced signal associated with the expansion of the Hadley Cell has emerged above the
175 noise of internal variability in the Southern Hemisphere in the 2000-2010 decade.

176 There is an evident seasonality in the projected large scale circulation anomalies over the
177 South Atlantic Ocean and south of SSA, with the most evident forced signals in April-May and
178 August-September (Fig. 5). Positive anomalies of mean sea level pressure are overall sug-
179 gestive of a poleward shift of the Hadley cell. Projected changes in the 300 hPa eddy kinetic
180 energy (a proxy for the storm track) show a southward shift of the midlatitude storm track in
181 AM and AS, but not JJ. Indeed, the weakest forced signals are projected in SPEAR_MED at
182 the peak of the rainy season in June-July (Fig. 5), consistent with the decadal forced mean
183 sea level pressure signals in the 2010-20 decade (SI Appendix, Fig. S9) and with the percent

184 WRI reductions (SI Appendix, Fig. S8b). Remarkably, the 2015-2017 meteorological drought
185 was also driven mainly by April-May and August-September rainfall deficits, associated with
186 large scale anomalies more evident in, e.g., April-May, and similar to those just described
187 above^{3,4,6}. These seasonal aspects of the Southern Hemisphere forced circulation changes
188 coherently suggest that future meteorological droughts might indeed have a similar seasonal
189 evolution as that in 2015-2017.

190 **Comparison with other large ensembles**

191 We analyzed additional large ensembles from coupled models with the same or coarser res-
192 olution that can provide an important context to our results and inform us about uncertainties
193 due to model differences^{32,39}: SPEAR_LO, the Forecast-Oriented Low Ocean Resolution
194 model with (FLOR_FA) and without (FLOR) flux adjustment, the Community EARTH Sys-
195 tem Model Large Ensemble, CESM-LENS³⁰, and the Max Planck Institute Grand Ensemble,
196 MPI-GE²⁶ (see Methods and SI Appendix for the evaluation of these models).

197 All models suggest a substantial rainfall reduction (SI Appendix, Figs. S8b, S11, S12),
198 with CESM-LENS and MPI-GE projecting a percent precipitation reduction pretty uniform
199 throughout AMJJAS. Mean sea level pressure changes are overall suggestive of a poleward
200 expansion of the descending branch of the Hadley Cell (SI Appendix, Fig. S10), but with
201 anomaly patterns that are more consistent across models in April-May and less consistent in
202 June-September. Indeed, the Subtropical Anticyclone response in the Southern Hemisphere
203 features larger intermodel uncertainty in the austral winter⁴⁰. A more prolonged dry season
204 into the late austral fall (AM) over SSA is therefore a robust indication in terms of future
205 precipitation reduction and droughts risk.

206 Relative to SPEAR_MED, the risk estimate is lower in SPEAR_LO (Fig. 2g), while FLOR
207 suggests similar values. MPI-GE, FLOR_FA and CEMS-LENS have a risk ratio larger than
208 SPEAR_MED by a factor 1.5, 1.8 and 2.8, respectively. By the end of this century, all models

209 agree on a probability of occurrence for the event_1517 at least ninety times larger than in
210 the twentieth century (Fig. 2h) under the highest emission scenarios (SSP5-8.5 or RCP8.5).
211 Middle-of-the-road scenarios (SSP2-4.5 or RCP4.5) tend to suggest a risk ratio of about
212 thirty, while the low-emission RCP2.6 scenario (only available for MPI-GE), aiming to limit
213 the increase of global mean temperature to 2 K, project a risk ratio of about 13.

214 **Conclusions**

215 The use of a new high-resolution large ensemble provides a significantly improved ability
216 to simulate regional-scale SSA droughts in both present and future conditions despite large
217 internal climate variability. We find that the rainfall deficit that led to the Day Zero drought
218 was 5.5 times more likely due to anthropogenic climate change, with a confidence interval of
219 [4,8]. We therefore are able, through the use of a model with higher resolution and better cli-
220 matology, to further constrain the risk ratio of SSA drought at and above the original [1.4,6.4]
221 estimate from ref.⁵. This highlights the usefulness of high resolution climate models to study
222 future drought risk and provides additional guidance to design water management to avoid
223 extreme drought.

224 Looking at the future, our results point to a dramatic increase in the risk of meteorological
225 droughts of similar or even more serious magnitude by the end of the twenty-first century.
226 Similarly to what occurred in 2015-2017, this increased risk of meteorological droughts is
227 associated with a substantial rainfall reduction, especially in the shoulder season (April-May
228 and August-September).

229 A high-emission and intermediate-emission future scenario are analyzed, highlighting
230 that while there is uncertainty in the increase in drought risk due to future uncertainty in
231 forcings, both scenarios lead to substantial increases, such that a drought becomes a com-
232 mon occurrence. Combined with the likelihood of increased water demand due to a growing
233 population³ and increased evaporation due to higher temperatures⁴¹, the more frequent oc-

234 currence of wintertime droughts will likely present a major challenge for managing water
235 resources in the region without adaptation and preparation. While these results are for SSA,
236 such shifts in drought risk are likely to occur in other arid locations with variable precipitation
237 and large scale circulation shifts increasing the likelihood of multi-year extreme droughts.
238 These methods could then be applied elsewhere to identify emerging drought risks.

239 **Methods**

240 **SPEAR model and experiments**

241 The main conclusions of this study are obtained from the **S**eamless System for **P**rediction
242 and **E**Arth System **R**esearch (SPEAR)³³. SPEAR represents the newest modeling system
243 for seasonal to multidecadal prediction which incorporates new model development compo-
244 nents that have occurred in the last decade at NOAA Geophysical Fluid Dynamics Labo-
245 ratory. These include: a new dynamical core⁴², revised atmospheric physics⁴³, a new sea
246 ice and ocean model⁴⁴ and an enhanced land model⁴⁵. The SPEAR atmospheric model
247 uses 33 levels in the vertical and is run at different atmospheric-land horizontal resolutions:
248 0.5°(SPEAR_MED) and 1° (SPEAR_LO) in this paper. The intermediate 0.5° configuration,
249 SPEAR_MED, is a compromise between the possibility to run a large ensemble of simu-
250 lations with available computation resources and retaining enough horizontal resolution to
251 study regional climate and extremes. It is worth noting that the SPEAR_MED large en-
252 semble features a horizontal grid-spacing (0.5°) that is finer than those used in most of the
253 previously used large ensembles (with the exception of FLOR,³¹), thus making these GFDL
254 ensembles a unique and unprecedented tool to study extremes and regional climate.

255

256 We use four different numerical experiments: (1) a long-term control simulation (CTRL)

257 to evaluate unforced natural variability; (2) an ensemble driven by natural forcing only (NAT-
258 URAL) to provide a baseline with only natural forcing (i.e., volcanic eruptions and solar cy-
259 cles); (3) an ensemble driven by observed natural and anthropogenic forcing up to 2014
260 (HIST) and then according to the intermediate ($\approx +3$ K of global warming by the end of the
261 twenty-first century) Shared Socioeconomic Pathway (SSP2-4.5) developed for the Cou-
262 pled Model Intercomparison Project Phase 6 (CMIP6)^{35,46}; and (4) an ensemble driven by
263 observed natural and anthropogenic forcing up to 2014 (HIST) and then according to the
264 CMIP6 high-emission, fossil fuel dominated ($\approx +5$ K of global warming by the end of the
265 twenty-first century) Shared Socioeconomic Pathway (SSP5-8.5).

266 The 3000-year CTRL simulation is driven by CO₂ forcing kept constant at 1850 levels.
267 Climate drifts associated with this long-term integrations are estimated to be very small and
268 statistically insignificant for the winter SA rainfall. The 30 members of the NATURAL en-
269 semble are driven by the same observed natural forcing (i.e., solar and volcanic) until year
270 2014, and by only solar forcing (quasi-11-year cycle) after 2014, with the anthropogenic
271 forcing held fixed at the 1921 level. In the HIST+SSP5-8.5 (HIST+SSP2-4.5) ensemble,
272 each member is driven by observed natural and anthropogenic forcing (greenhouse gases,
273 anthropogenic aerosols, ozone) up to year 2014, and by the SSP5-8.5 (SSP2-4.5) forcing
274 afterwards. More details about how the SPEAR large ensemble is designed can be found in
275 Delworth et al. (2020)³³.

276

277 **Model Evaluation**

278 In addition to the model's ability to reproduce the wintertime southern African climatology
279 (Fig. 1c-e), the performance of SPEAR_MED in simulating wintertime rainfall variability and
280 historical trends (1951-2017) over SSA is evaluated against three different observational
281 land rainfall datasets: the Global Precipitation Climatology Centre (GPCC) dataset⁴⁷ version

282 7, the Climate Research Unit high-resolution grids of monthly rainfall at the University of
283 East Anglia⁴⁸, version 3.24, and the University of Delaware (UDEL) precipitation dataset,
284 version 5 (<http://climate.geog.udel.edu/~climate/>), all at 0.5° resolution. The choice of these
285 three gridded observed datasets, in place of scattered measurements from the South African
286 Weather Service meteorological stations, is dictated by the need to be able to compare mod-
287 els with observations, as done in previous studies⁵. The values of these three precipitation
288 datasets for SSA are obtained from a limited number of stations and different interpola-
289 tion algorithms. As a consequence, they can feature, locally, considerable differences (e.g.,
290 Fig. 1a and SI Appendix, Fig. S1). However, differences in area-averaged metrics like, e.g.,
291 the WRI, are minimal (Fig. 1b), thus making our results independent from the choice of the
292 single precipitation dataset.

293 In order to have a realistic representation of the width of the distribution of rainfall anoma-
294 lies, it is key that SPEAR_MED reproduces the interannual, multiannual and decadal natural
295 variability of the SSA winter rainfall. To check this, we work out the standard deviation of the
296 detrended full, three-year and ten-year low-pass-filtered WRI from the three observational
297 datasets and the SPEAR_MED ensemble members over the common period 1921-2010 (SI
298 Appendix, Fig. S3). The standard deviation of the observations is between 5 mm month⁻¹
299 (CRU) and 6 mm month⁻¹ (GPCC, UDEL) for the three-year low-pass-filtered WRI. The stan-
300 dard deviation values from the model range from 4 to 6.3 mm month⁻¹. The observed values
301 are therefore within the range from the model, suggesting that the model has the ability to
302 properly estimate the magnitude of three-year lasting droughts. Similarly, a good agreement
303 between SPEAR_MED and observations exist for the standard deviations calculated from
304 the unfiltered WRI time series (interannual variability) and from ten-year low-pass-filtered
305 WRI (decadal and longer variability) too.

306 The effect of internal natural variability is large for SSA winter rainfall²⁷⁻²⁹, thus it is not
307 appropriate to compare observed AMJJAS rainfall trends directly with the ensemble mean

308 or with each single ensemble member, which may show contrasting signs (SI Appendix,
309 Fig. S2). Instead, we evaluate if SPEAR_MED's historical trends of AMJJAS rainfall are
310 consistent with observations over SSA. To do so, we compute rainfall trends over the last 67
311 years (1951-2017) in GPCC, CRU and UDEL, and compare them with individual members
312 of the HIST+SSP5-8.5 ensembles over the same time period.

313 If the observed trend at one grid point is within the range of those simulated by the 30
314 HIST ensemble members, then we say that the model is consistent with observations in that
315 grid box. We find that SPEAR_MED is consistent with observations over most of southern
316 Africa (SI Appendix, Fig. S13).

317 **Additional large ensembles**

318 To assess the robustness and model-dependence of our results, we analyze five additional
319 large ensembles (see Table S1): (1) the SPEAR_LO ensemble³³, (2) the GFDL Forecast-
320 Oriented Low Ocean Resolution (FLOR) model, at 0.5° land/atmosphere resolution, (3) the
321 flux-adjusted FLOR (FLOR_FA) large ensembles, obtained imposing temperature and salin-
322 ity flux adjustments at the ocean surface to FLOR⁴⁹ (both with a land-atmospheric horizon-
323 tal resolution of 0.5°), (4) the Community EARTH System Model Large Ensemble, CESM-
324 LENS³⁰, with land-atmospheric horizontal resolution of approximately 1°, and (5) the Max
325 Planck Institute Grand Ensemble, MPI-GE²⁶, with land-atmospheric horizontal resolution of
326 1.8°. These additional large ensembles are available with various CMIP5 scenarios and are
327 documented in Table S1. An evaluation of the wintertime climatology over SSA shows that
328 these models all underestimate AMJJAS mean rainfall (Fig 1c-e and SI Appendix, Fig. S14
329 and Table S2). With the exception of SPEAR_LO, these models also underestimate the
330 standard deviation of the full three-year and ten-year low-pass-filtered Winter Rainfall In-
331 dex (SI Appendix, Fig. S3). Critically, this means they also underestimate the width of the
332 probability distribution of the three-year AMJJAS rainfall anomalies (SI Appendix, Fig. S15).

333 In particular, CESM-LENS and FLOR_FA have standard deviations that are 50% and 40%
334 smaller, respectively, suggesting that they are poor tools for risk analysis over SSA. As they
335 substantially underestimate the probability of occurrence of event_1517, to quantify changes
336 in risk in a manner that implicitly account for model biases we use a three-year Winter Rain-
337 fall Index anomaly corresponding to the 1st percentile, which is the percentile to which -11.5
338 mm/month corresponds to in observations and SPEAR_MED.

339 **Winter Rainfall Index**

340 In this study we focus on the regional scale drought of the Western Cape. We thus use the
341 annual time series of the Winter Rainfall Index (WRI)²⁹ to monitor interannual variability and
342 monthly rainfall anomalies. To define the WRI, we first select the grid points where at least
343 65% of the total annual rainfall occur from April to September (Fig. 1c-e) and SI Appendix,
344 Fig. S13. Then, we take the areal mean of the extended winter (i.e., April-September) rain-
345 fall over the irregular region defined above (Fig. 1c-e, SI Appendix, Fig. S13). The WRI is
346 thus the area-averaged rainfall over the portion of SSA that experiences a dry summer and
347 a wet winter, that is a Mediterranean rainfall regime. This area encompasses the region of
348 intensely irrigated agriculture surrounding the metropolitan area of Cape Town as well as the
349 water basins of the Breede and Berg Rivers, where dams supplying water to Cape Town are
350 located.

351

352 **Detectability of the mean rainfall change**

353 To determine where and when the decadal changes in AMJJAS rainfall starts being caused
354 by external forcing and not by multidecadal variability, we apply a Monte Carlo approach to
355 the long CTRL run: at each grid box, we randomly choose a 10-yr period and a nonover-
356 lapping 50-yr period (to mimic 1921-1970). Then, we compute the time mean difference

357 between the 10-yr and 50-yr time series. This difference is solely associated with internal
358 natural variability of the climate system. This process is repeated 30 times (to mimic the
359 30-member ensemble), we then take the ensemble mean of these differences. The whole
360 process is then repeated 10,000 times to create an empirical probability distribution of these
361 ensemble mean differences, which is used to assess the detectability of decadal changes
362 in rainfall. Anomalies outside the range of the distribution are attributed to external forcing
363 and considered detectable against internal climate variability (Fig. 4 and SI Appendix, Figs.
364 S11-S12).

365 **Estimation of the probability distribution**

366 We derive a probability distribution of the three-year mean WRI anomalies due to natural
367 variability alone from the long CTRL run. We randomly select a 50-year and three-year
368 sequence (non-overlapping), and then calculate the anomaly of the three-year period relative
369 to the 50-year climatology. This choice mimics the 2015-2017 mean minus the 1921-1970
370 mean. We repeat this process N times (N=10,000) to form a distribution of the three-year
371 WRI anomalies (Fig. 2a-d). The probability of occurrence of experiencing a three-year WRI
372 anomaly equal to or less than the 2015-2017 anomaly – as per the gridded datasets – is
373 about 1% in CTRL, and 0.7% from HIST taking the average of decadal probabilities over
374 1921-1970, respectively (Fig. 2e). Similarly, we estimate the distribution of the four-year
375 WRI anomaly. The probability of occurrence of a WRI anomaly of the same intensity but of
376 one additional year of duration is 0.4% and 0.2% from the CTRL and HIST, respectively.

377 To evaluate the decadal change in the probability of occurrence of a three-year WRI
378 anomaly equal to or worse than that of 2015-17, we empirically estimate a decadal-varying
379 probability distribution using the HIST and SSP5-8.5 (SSP2-4.5) experiments. The probabil-
380 ity distribution is estimated for a 20-year time window, so that, for example, that referred to
381 2010 is built from all years from 2001 to 2020. This choice is motivated by the need to have

382 a time period not too wide in order to assume the stationarity of the probability distribution,
383 but at the same time a number of instances large enough to allow for sufficiently accurate
384 estimates of probabilities of rare events (e.g., 100-year return time). In a 20-year time win-
385 dow there are eighteen different three-year WRI anomalies (relative to the climatological
386 reference period 1921-1970). This leads to $18 \times 30 = 540$ different values when considering
387 all the 30 ensemble members, from which we empirically build the decadal probability dis-
388 tribution. Once we have decadal probability distribution, we can estimate the probability of
389 occurrence, for each bi-decadal period, of three-year WRI anomaly equal to or less than that
390 observed in 2015-2017 ($-11.5 \text{ mm month}^{-1}$, obtained averaging GPCP, CRU and UDEL) for
391 any random three year segment within the 20-year time window. The 95% confidence inter-
392 val in these probabilities are estimated by applying bootstrap-with-replacement resampling
393 10,000 times. The same methodology is applied to estimate the probability of occurrence of
394 four-year droughts.

395 We quantify the uncertainty in the estimate of the decadal probability of occurrence, de-
396 rived from only 540 different three-year rainfall anomaly values, as follows: we take the long
397 3,000-year CTRL and randomly select a 50-year and three-year non-overlapping periods
398 and estimate the difference. We repeat this step N times (with $N=10,000$) to obtain a large
399 population sample of N three-year anomalies, from which the probability of the event_1517
400 is estimated to be $\approx 1\%$. From this large sample we then randomly draw M realizations (with
401 replacement), with $M \leq N$ and estimate the probability of occurrence. For each value of M
402 we repeat the last step 10,000 times and obtain 10,000 different probability estimates which
403 allows us to estimate the 95% confidence interval (SI Appendix, Fig. S4b). As expected, the
404 confidence interval decreases with M up to approximately [0.9%,1.2%] for $M=10,000$. For
405 values of M less than 300, the uncertainty is so large that it is impossible to have any sensible
406 estimate of the probability of the event. For $M=540$, the confidence interval is approximately
407 [0.5%,1.7%], which we can consider sufficiently accurate for our purposes.

408 **Joint probability distribution of drought intensity and duration**

409 The probability distribution of a drought in the Cape Town's Mediterranean area as a func-
410 tion of duration and intensity is estimated from the historical and projected AMJJAS WRI
411 anomaly time series. The focus in this paper is on severe droughts, therefore we select, for
412 each time series, all contiguous years for which the WRI anomaly is below -0.75 standard
413 deviation ($\approx -6 \text{ mm month}^{-1}$). With this choice we exclude years that were moderately and
414 very moderately dry. For each of these segments, we work out the mean WRI anomaly by
415 averaging the annual WRI anomaly values over the whole segment. We choose a 2 mm
416 $\text{month}^{-1} \times 1 \text{ year}$ bin (Fig. 3) to work out the percentage of the droughts within each bin.
417 The analysis is performed for the 1921-1970 time period, and for the periods 2011-2040,
418 2041-2070, 2071-2100. To evaluate if the probability differences relative to 1921-1970 are
419 attributable to anthropogenic climate change, we apply the same method to the 3,000-year
420 CTRL. We randomly select a 50-year and a 30-year non-overlapping time spans, and com-
421 pute the number of droughts for each duration-drought intensity bin. We repeat this 30 times
422 to mimic the 30-member ensemble and so work out the probability differences between the
423 50-year and 30-year periods. The whole process is then repeated 10,000 times to create an
424 empirical probability distribution of the probability differences for each bin: anomalies out-
425 side the range of the distribution are attributed to external forcing and considered detectable
426 against internal climate variability.

427 **Acknowledgements**

428 We thank A. T. Wittenberg, H. Murakami, P. C. D. Milly and two anonymous reviewers for their
429 comments and suggestions. This report was prepared by S. P. under award NA18OAR4320123
430 from the National Oceanic and Atmospheric Administration, U.S. Department of Commerce.
431 The statements, findings, conclusions, and recommendations are those of the author(s) and

432 do not necessarily reflect the views of the National Oceanic and Atmospheric Administration,
433 or the U.S. Department of Commerce.

434 **Authors' contributions**

435 S. P. conceived the study, performed the analysis and wrote the initial draft of the paper. T.
436 L. D. and W. F. C. designed the ensemble, and W. F. C performed the numerical simulations.
437 All authors took part in the discussion of the results and contributed to the writing.

438 **Competing interests**

439 The authors declare no competing interests.

440 **References**

- 441 [1] Archer E., W. Landman, J. Malherbe, M. Tadross, and S. Pretorius. South Africa's winter
442 rainfall region drought: A region in transition? *Climate Risk Management*, 25:100188,
443 2019.
- 444 [2] Parks R., M. McLaren, R. Toum, and U. Rivett. Experiences and lessons in managing
445 water from Cape Town. *Grantham Institute Briefing paper*, 29:1–18, 2019.
- 446 [3] Sousa P. M., Blamey R. C., Reason C. J. C., Ramos A. M., and R. M. Trigo. The 'Day
447 Zero' Cape Town drought and the poleward migration of moisture corridors. *Env. Res.
448 Lett.*, 13:124025, 2018.
- 449 [4] Burls N. J., R. C. Blamey, B. A. Cash, E. T. Swenson, A. al Fahad, M.-J. M. Bopape,
450 D. M. Straus, and C. J. C. Reason. The Cape Town "Day Zero" drought and Hadley cell
451 expansion. *npj Climate and Atmospheric Science*, 2:2–27, 2019.
- 452 [5] Otto F. E. L., P. Wolski, F. Lehner, C. Tebaldi, G. J. van Oldenborgh, S. Hogesteege,
453 R. Singh, P. Holden, N. S. Fučkar, and R. C. Odoulami. Anthropogenic influence on the
454 drivers of the Western Cape drought 2015-2017. *Environ. Res. Lett.*, 13:124010, 2018.

- 455 [6] Mahlalela P.T., R. C. Blamey, and C. J. C. Reason. Mechanisms behind early winter
456 rainfall variability in the southwestern Cape, South Africa. *Clim. Dyn.*, 53:21–39, 2019.
- 457 [7] City of Cape Town. Water Outlook 2018 (Rev. 25) 20 May 2018. *Department of Water
458 and Sanitation*, pages 1–16, 2018.
- 459 [8] Simpkins G. Running dry. *Nat. Clim. Change*, 8:369–369, 2018.
- 460 [9] Wolski P. How severe is Cape Town’s “Day Zero” drought? *Significance*, 15:24–27,
461 2018.
- 462 [10] Muller M. Cape Town’s drought: don’t blame climate change. *Nature*, 559:174–176,
463 2018.
- 464 [11] Bischoff-Mattson Z., G. Maree, C. Vogel, A. Lynch, D. Olivier, and D. Terblanche. Shape
465 of a water crisis: practitioner perspectives on urban water scarcity and “Day Zero” in
466 South Africa. *Water Policy*, 22(2):193–210, 2020.
- 467 [12] Huang J., Y. Li, C. Fu, F. Chen, Q. Fu, A. Dai, M. Shinoda, Z. Ma, W. Guo, Z. Li,
468 L. Zhang, Y. Liu, H. Yu, Y. He, Y. Xie, X. Guan, M. Ji, L. Lin, S. Wang, H. Yan, and
469 G. Wang. Dryland climate change: Recent progress and challenges. *Rev. Geophys.*,
470 55:719 – 778, 2017.
- 471 [13] Lehner F., S. Coats, T. F. Stocker, B. M. Sanderson, A. G. Pendergrass, C. C. Raible,
472 and J. E. Smerdon. Projected drought risk in 1.5° C and 2° C warmer climates. *Geo-
473 physical Research Letters*, 44:7419–7428, 2017.
- 474 [14] Cook B. I., J. E. Smerdon, R. Seager, and S. Coats. Global warming and 21st century
475 drying. *Climate Dynamics*, 43:2607–2627, 2014.
- 476 [15] Lu J., G. A. Vecchi, and T. Reichler. Expansion of the Hadley cell under global warming.
477 *Geophys. Res. Lett.*, 34:L06805, 2007.
- 478 [16] Amaya D. J., N. Siler, S.-P. Xie, and A. J. Miller. The interplay of internal and forced
479 modes of Hadley Cell expansion: lessons from the global warming hiatus. *Clim Dyn*,
480 51:305–319, 2018.

- 481 [17] Staten P. W., J. Lu, K. M. Grise, S. M. Davis, and T. Birner. Re-examining tropical
482 expansion. *Nat. Clim. Change*, 8:768–775, 2018.
- 483 [18] Grise K.M., S.M. Davis, I.R. Simpson, D.W. Waugh, Q. Fu, R.J. Allena, K.H. Rosenlof,
484 C.C. Ummenhofer, K.B. Karnauskas, A.C. Maycock, X. Quan, T. Birner, and P.W. Staten.
485 Recent Tropical Expansion: Natural Variability or Forced Response? *J. Climate*,
486 32:1551–1571, 2019.
- 487 [19] Curtis P. E., P. Ceppi, and G. Zappa. Role of the mean state for the southern hemi-
488 spheric jet stream response to CO₂ forcing in CMIP6 models. *Environ. Res. Lett.*,
489 15:064011, 2020.
- 490 [20] Meehl G. A., C. Covey, T. Delworth, M. Latif, B. McAvaney, J. F. B. Mitchell, R. J. Stouffer,
491 and K. E. Taylor. THE WCRP CMIP3 multimodel dataset: A new era in climate change
492 research. *Bull. Amer. Meteor.*, 88:1383–1394, 2007.
- 493 [21] Taylor K. E., R. J. Stouffer, and G. A. Meehl. An overview of CMIP5 and the experiment
494 design. *Bull. Amer. Meteor.*, 93:485–498, 2012.
- 495 [22] Kidston J. and E. P. Gerber. Intermodel variability of the poleward shift of the austral jet
496 stream in the CMIP3 integrations linked to biases in 20th century climatology. *Geophys.*
497 *Res. Lett.*, 37:L09708, 2010.
- 498 [23] Ceppi P., Y. T. Hwang, D. M. W. Frierson, and D. L. Hartmann. Southern Hemisphere
499 jet latitude biases in CMIP5 models linked to shortwave cloud forcing. *Geophys. Res.*
500 *Lett.*, 39:L19708, 2015.
- 501 [24] Li C., F. Zwiers, X. Zhang, and G. Li. How much information is required to well constrain
502 local estimates of future precipitation extremes? *Earth's Future*, 7:11–24, 2019.
- 503 [25] Van der Wiel K., N. Wanders, F. M. Selten, and M. F. P. Bierkens. Added value of large
504 ensemble simulations for assessing extreme river discharge in a 2° C warmer world.
505 *Geophysical Research Letters*, 46:2093–2102, 2019.
- 506 [26] Maher N., S. Milinski, L. Suarez-Gutierrez, M. Botzet, M. Dobrynin, L. Kornblueh,

- 507 J. Kröger, Y. Takano, R. Ghosh, C. Hedemann, C. Li, H. Li, Elisa Manzini, D. Notz, D. Pu-
508 trasahan, L. Boysen, M. Claussen, T. Ilyina, D. Olonscheck, T. Raddatz, B. Stevens, and
509 J. Marotzke. The Max Planck Institute Grand Ensemble: Enabling the Exploration of
510 Climate System Variability. *Journal of Advances in Modeling Earth Systems*, 11:2050–
511 2069, 2019.
- 512 [27] Philippon N., M. Rouault, Y. Richard, and A. Favre. The influence of ENSO on winter
513 rainfall in South Africa. *Int. J. Climatol.*, 32:2333–2347, 2012.
- 514 [28] Reason C., M. Rouault, J. Melice, and D. Jagadheesha. Interannual winter rainfall
515 variability in SW South Africa and large scale ocean-atmosphere interactions. *Meteorol.*
516 *Atmos. Phys.*, 80:19–29, 2002.
- 517 [29] Dieppois B., B. Pohl, M. Rouault, M. New, D. Lawler, and N. Keenlyside. Interannual
518 to interdecadal variability of winter and summer southern African rainfall, and their tele-
519 connections. *J. Geophys. Res. Atmos.*, 121:6215–6239, 2016.
- 520 [30] Kay J. E., C. Deser, A. Phillips, A. Mai, C. Hannay, G. Strand, J.M. Arblaster, S.C.
521 Bates, G. Danabasoglu, J. Edwards, M. Holland, P. Kushner, J. Lamarque, D. Lawrence,
522 K. Lindsay, A. Middleton, E. Munoz, R. Neale, K. Oleson, L. Polvani, and M. Vertenstein.
523 The Community Earth System Model (CESM) Large Ensemble Project: A community
524 resource for studying climate change in the presence of internal climate variability. *Bull.*
525 *Amer. Meteor. Soc.*, 96:1333–1349, 2015.
- 526 [31] Zhang H. and T. Delworth. Detectability of Decadal Anthropogenic Hydroclimate
527 Changes over North America. *J. Climate*, 31:2579–2597, 2018.
- 528 [32] Deser C., F. Lehner, K. B. Rodgers, T. Ault, T. L. Delworth, P. N. DiNezio, A. Fiore,
529 C. Frankignoul, J. C. Fyfe, D. E. Horton, J. E. Kay, R. Knutti, N. S. Lovenduski,
530 J. Marotzke, K. A. McKinnon, S. Minobe, J. Randerson, J. A. Screen, I. R. Simpson,
531 and M. Ting. Insights from Earth system model initial-condition large ensembles and
532 future prospects. *Nat. Clim. Change*, 10:277–286, 2020.

- 533 [33] Delworth T. L., W.F. Cooke, A. A. Adcroft, M. Bushuk, J.-H. Chen, K. A. Dunne, P. Gi-
534 noux, R. Gudgel, R. W. Hallberg, L. Harris, M. J. Harrison, N. Johnson, S. B. Kapnick,
535 S.-J. Lin, F. Lu, S. Malyshev, P. C. Milly, H. Murakami, V. Naik, S. Pascale, D. Paynter,
536 A. Rosati, M. D. Schwarzkopf, E. Shevliakova, S. Underwood, A.T. Wittenberg, B. Xi-
537 ang, X. Yang, F. Zeng, H. Zhang, L. Zhang, and M. Zhao. SPEAR - the next generation
538 GFDL modeling system for seasonal to multidecadal prediction and projection. *Journal*
539 *of Advances in Modeling Earth Systems*, 12:e2019MS001895, 2020.
- 540 [34] Held I.M., H. Guo, A. Adcroft, J. P. Dunne, L. W. Horowitz, J. Krasting, E. Shevliakova,
541 M. Winton, M. Zhao, M. Bushuk, A. T. Wittenberg, B. Wyman, B. Xiang, R. Zhang,
542 W. Anderson, V. Balaji, L. Donner, K. Dunne, J. Durachta, P. P. G. Gauthier, P. Ginoux,
543 J.-C. Golaz, S. M. Griffies, R. Hallberg, L. Harris, M. Harrison, W. Hurlin, J. John, P. Lin,
544 S.-J. Lin, S. Malyshev, R. Menzel, P. C. D. Milly, Y. Ming, V. Naik, D. Paynter, F. Paulot,
545 V. Rammawamy, B. Reichl, T. Robinson, A. Rosati, C. Seman, L. G. Silvers, S. Un-
546 derwood, and N. Zadeh. Structure and Performance of GFDL's CM4.0 Climate Model.
547 *Journal of Advances in Modeling Earth Systems*, 11:3691–3727, 2020.
- 548 [35] Eyring V., S. Bony, G. A. Meehl, C. A. Senior, B. Stevens, R. J. Stouffer, and K. E. Taylor.
549 Overview of the Coupled Model Intercomparison Project Phase 6 (CMIP6) experimental
550 design and organization. *Geoscientific Model Development*, 9:1937–1958, 2016.
- 551 [36] Milly P.C.D., J. Betancourt, M. Falkenmark, R. M. Hirsch, Z. W. Kundzewicz, D. P. Let-
552 tenmaier, and R. J. Stouffer. Stationarity is dead: whither water management? *Science*,
553 319:573–574, 2008.
- 554 [37] Jakob D. Nonstationarity in Extremes and Engineering Design. In AghaKouchak A.
555 and Easterling D. and Hsu K. and Schubert S. and Sorooshian S., editor, *Extremes in*
556 *a Changing Climate: Detection, Analysis and Uncertainty*, chapter 13, pages 363–417.
557 Springer, New York, 2013.
- 558 [38] Polade S. D., A. Gershunov, D. R. Cayan, M. D. Dettinger, and D. W. Pierce. Precipita-

- 559 tion in a warming world: Assessing projected hydro-climate changes in California and
560 other Mediterranean climate regions. *Sci. Rep.*, 7:10783, 2017.
- 561 [39] Hauser M., L. Gudmundsson, R. Orth, A. Jezequel, K. Haustein, R. Vautard, G. J.
562 van Oldenborgh, L. Wilcox, and S. I. Seneviratne. Methods and model dependency of
563 extreme event attribution: The 2015 European drought. *Earth's Future*, 5:1034–1043,
564 2017.
- 565 [40] Fahad A., N. J. Burls, and Z. Strasberg. How will southern hemisphere subtropical
566 anticyclones respond to global warming? Mechanisms and seasonality in CMIP5 and
567 CMIP6 model projections. *Clim. Dynam.*, 55:703–718, 2020.
- 568 [41] Milly P.C.D. and K. Dunne. Potential evapotranspiration and continental drying. *Nat.*
569 *Clim. Change*, 6:946–949, 2016.
- 570 [42] Harris L. M. and S.-J. Lin. A two-way nested global-regional dynamical core on the
571 cubed-sphere grid. *Monthly Weather Review*, 141:283–306, 2013.
- 572 [43] Zhao M., J.-C. Golaz, I. M. Held, H. Guo, V. Balaji, R. Benson, J.-H. Chen, X. Chen, L. J.
573 Donner, J. P. Dunne, K. Dunne, J. Durachta, S.-M. Fan, S. M. Freidenreich, S. T. Garner,
574 P. Ginoux, L. M. Harris, L. W. Horowitz, J. P. Krasting, A. R. Langenhorst, Z. Liang, P. Lin,
575 S.-J. Lin, S. L. Malyshev, E. Mason, P. C. D. Milly, Y. Ming, V. Naik, F. Paulot, D. Paynter,
576 P. Phillipps, A. Radhakrishnan, V. Ramaswamy, T. Robinson, D. Schwarzkopf, C. J.
577 Seman, E. Shevliakova, Z. Shen, H. Shin, L. G. Silvers, J. R. Wilson, M. Winton, A. T.
578 Wittenberg, B. Wyman, and B. Xiang. The GFDL Global Atmosphere and Land Model
579 AM4.0/LM4.0: 2. Model Description, Sensitivity Studies, and Tuning Strategies. *Journal*
580 *of Advances in Modeling Earth Systems*, 10:735–769, 2018.
- 581 [44] Adcroft A., W. Anderson, V. Balaji, C. Blanton, M. Bushuk, C. O. Dufour, J. P. Dunne,
582 S. M. Griffies, R. Hallberg, M. J. Harrison, I. M. Held, M. F. Jansen, J. G. John, J. P.
583 Krasting, A. R. Langenhorst, S. Legg, Z. Liang, C. McHugh, A. Radhakrishnan, B. G.
584 Reichl, T. Rosati, B. L. Samuels, A. Shao, R. Stouffer, M. Winton, A. T. Wittenberg,

- 585 B. Xiang, N. Zadeh, and R. Zhang. The GFDL global ocean and sea ice model OM4.0:
586 Model description and simulation features. *Journal of Advances in Modeling Earth*
587 *Systems*, 11, 2019.
- 588 [45] Milly P.C.D., S. L. Malyshev, E. Shevliakova, K. A. Dunne, K. L. Findell, T. Gleeson,
589 Z. Liang, P. Phillipps, R. J. Stouffer, and S. Swenson. An Enhanced Model of Land
590 Water and Energy for Global Hydrologic and Earth- System Studies. *Journal of Hy-*
591 *drometeorology*, 15:1739–1761, 2014.
- 592 [46] O’Neill B. C., E. Kriegler, K. L. Ebi, E. Kemp-Benedict, K. Riahi, D. S. Rothman, B. J.
593 van Ruijven, D. P. van Vuuren, J. Birkmann, K. Kok, M. Levy, and W. Solecki. The roads
594 ahead: Narratives for shared socioeconomic pathways describing world futures in the
595 21st century . *Global Environ. Chang.*, 42:169–180, 2017.
- 596 [47] U. Schneider, E. Becker, P. Finger, A. Meyer-Christoffer, M. Ziese, and B. Rudolf.
597 GPCP’s new land surface precipitation climatology based on quality-controlled in situ
598 data and its role in quantifying the global water cycle. *Theoretical and Applied Clima-*
599 *tology*, 115(1-2):15–40, 2013.
- 600 [48] Harris I., P.D. Jones, T. J. Osborn, and D. H. Lister. Updated high-resolution grids of
601 monthly climatic observations – the CRU TS3.10 Dataset. *Int. J. Climatol.*, 34:623–642,
602 2013.
- 603 [49] Vecchi G.A., T. Delworth, R. Gudgel, S. Kapnick, A. Rosati, A.T. Wittenberg, F. Zeng,
604 W. Anderson, V. Balaji, K. Dixon, L. Jia, H. Kim, L. Krishnamurthy, R. Msadek, W.F.
605 Stern, S.D. Underwood, G. Villarini, X. Yang, and S. Zhang. On the Seasonal Forecast-
606 ing of Regional Tropical Cyclone Activity. *J. Climate*, 27:7994–8016, 2014.

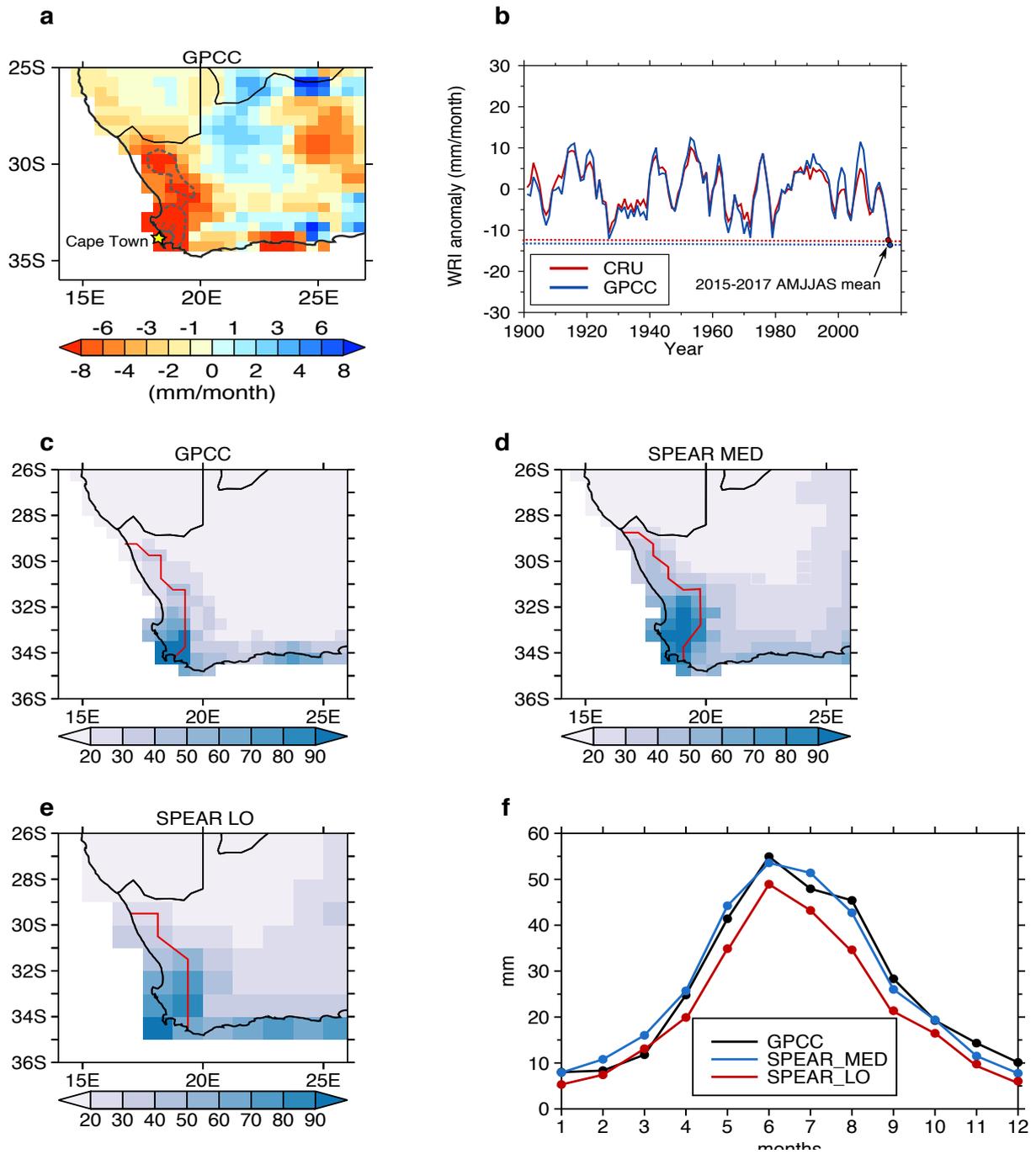


Figure 1: **a**, Mean 2015-2017 AMJJAS rainfall anomaly relative to 1921-1970. The dashed (continuous) line denotes negative anomalies beyond 1 (1.5) standard deviation. **b**, Time series of the observed (GPCC, blue; CRU, red) 3-yr running mean AMJJAS Winter Rainfall Index (WRI, see Methods) from 1901 to 2017. The 2015-2017 mean is a record-breaking over the period 1901-2017. Mean 1921-1970 AMJJAS rainfall (mm/month) in **c**, observations (GPCC), **d**, SPEAR_MED, and **e**, SPEAR_LO. The red lines encircle the area receiving at least 65% of the total annual rainfall during AMJJAS used to define WRI. **f**, Monthly WRI in observations and models. Comparison of SPEAR_MED with SPEAR_LO shows how an enhanced resolution is key to capture finer scale regional details of winter rainfall in the relatively small SSA Mediterranean region.

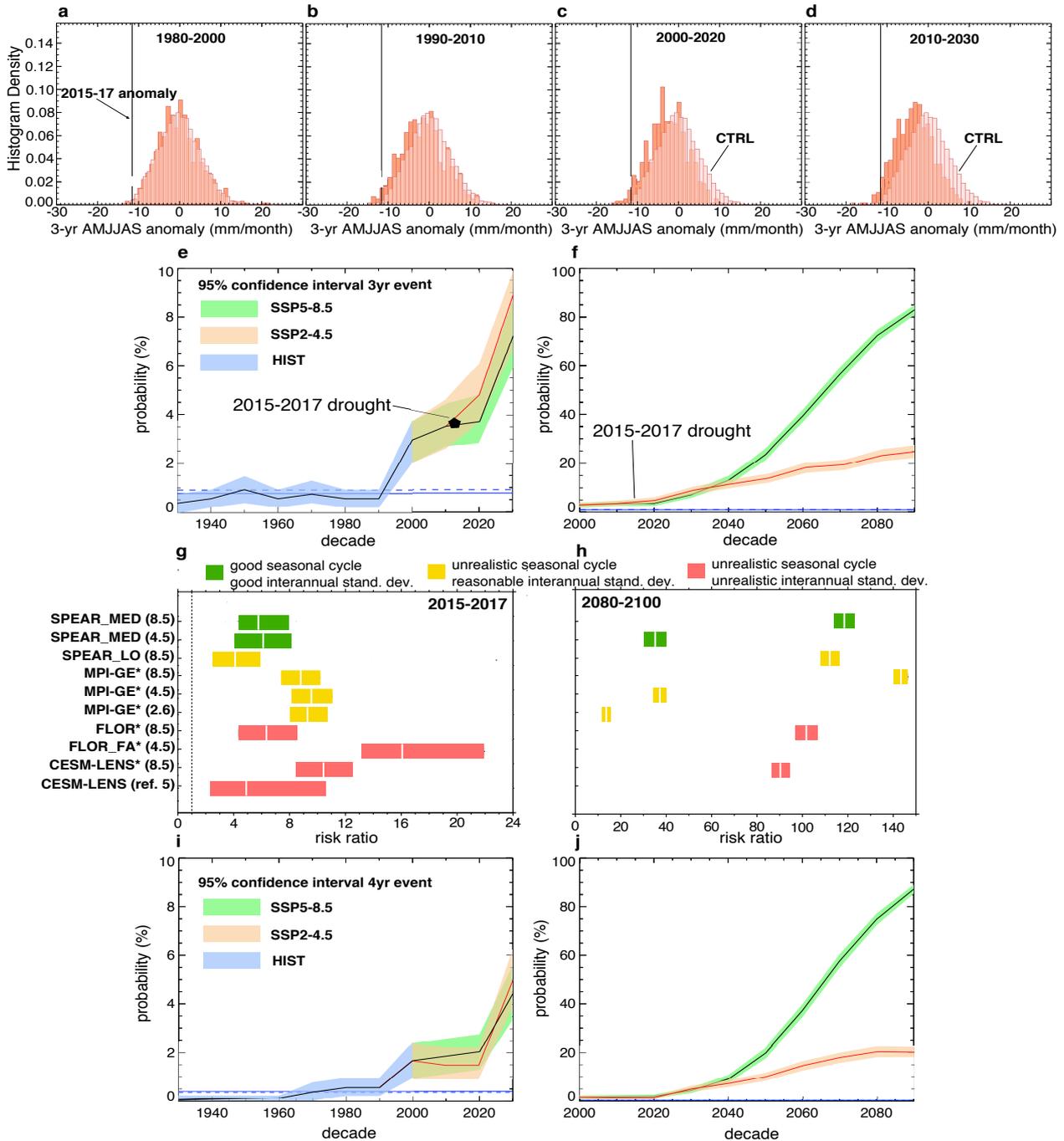


Figure 2: a, Empirical probability distribution of the three-year winter rainfall anomalies due to internal variability alone (light pink, from CTRL) and natural variability, natural forcing and anthropogenic forcing (salmon, from SSP5-8.5) in the period 1980-2000 b, 1990-2010. c, 2000-2020. d, and 2010-2030. Black vertical lines represent the 2015-2017 AMJJAS rainfall anomaly (-11.5 mm/month, averaged value across GPCP, CRU, UDELAW). e, and f, Decadal probability of occurrence of a three-year winter rainfall anomaly equal to or worse than in 2015-2017 in HIST, SSP2-4.5 and SSP5-8.5. Shading denotes the 95% confidence interval from bootstrap resampling. The blue constant line denotes the CTRL probability for such an event, and the blue constant dashed line that from the NATURAL run after concatenating all 30 ensemble members. g, Probability (risk) ratios (to the mean 1921-1980) with 95% uncertainty intervals for event_1517 in 2015-2017, and h, at the end of the 21st century (2080-2100). Models are top-down ordered from the most skillful in reproducing WRI variability and seasonal cycle (SI Appendix, Fig. SS and Table S2). Asterisk (*) denotes models for which a relative threshold (1st percentile) is used to estimate the probability (see Methods). i, and j as in e, f but for a four-year anomaly of the magnitude of the 2015-2017 drought.

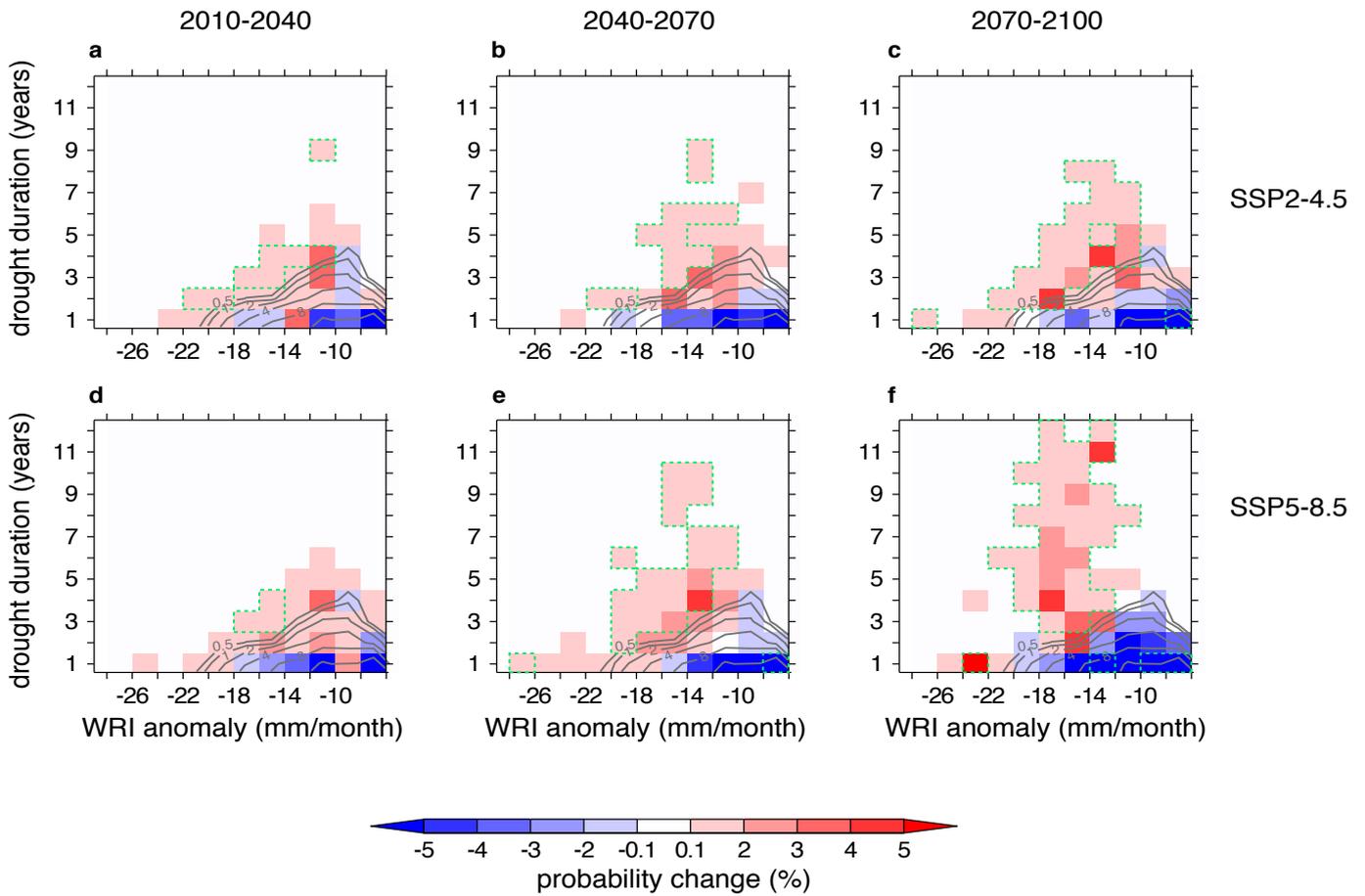


Figure 3: Change of probability of large annual AMJJAS rainfall anomalies ($\leq -0.5\sigma$) as a function of duration (years) and intensity (mean WRI anomaly over the drought duration period) for the, **a**, 2010-2040 period relative to 1921-1970 baseline (contours), **b**, 2040-2070 period, and, **c**, 2070-2100 period under SSP2-4.5. Green dashed line encircles values that are outside the range of natural variability. **d-f** As in **a-c** but for the SSP5-8.5 pathway.

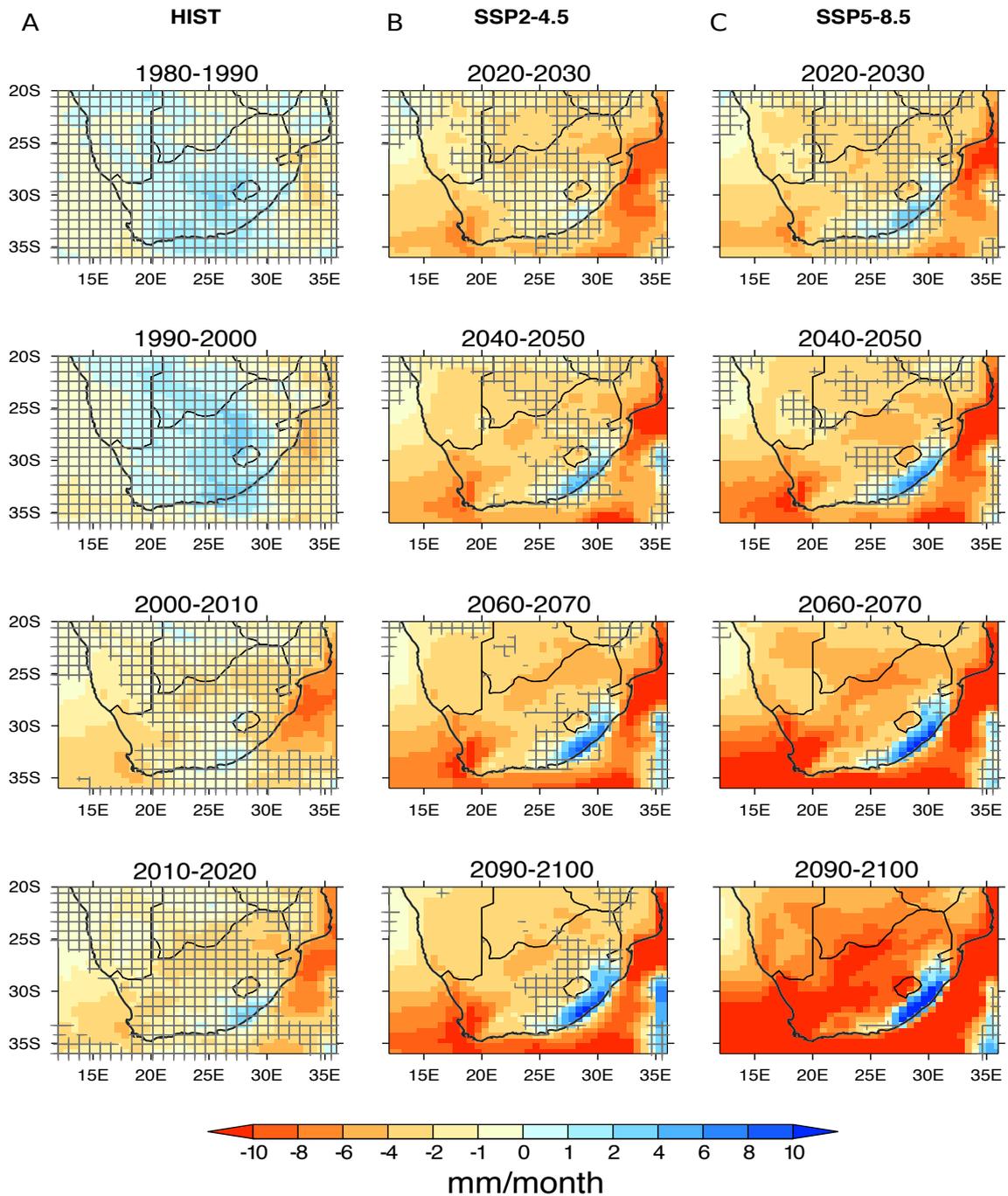


Figure 4: Decadal evolution of wintertime (AMJJAS) rainfall mean anomalies (ensemble average, shading) relative to the 1921-1970 climate from the **a**, HIST, **b**, SSP2-4.5. and **c**, SSP5-8.5 runs. Gray crosses denote changes in wintertime rainfall mean state that are not distinguishable from internal climate variability as estimated from fully coupled control simulations (see Methods for details).

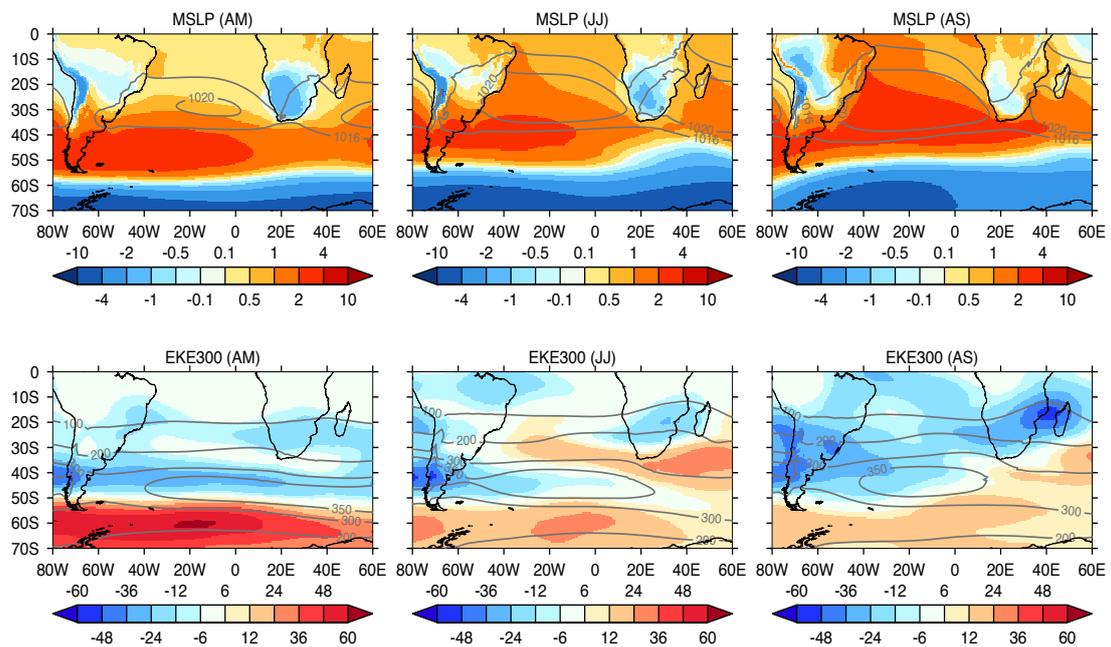


Figure 5: Ensemble mean anomalies (shading) of April-May (AM), June-July (JJ) and August-September (AS) sea level pressure (upper row; hPa) and 300-hPa eddy kinetic energy ($m^2 s^{-2}$) for the period 2071-2100 relative to 1921-1970. Contours denote the 1921-1970 climatological values.